

Engineering the microwave to infrared noise photon flux for superconducting quantum systems

Sergey Danilin,^{1,*} João Barbosa,¹ Michael Farage,¹ Zimo Zhao,¹ Xiaobang Shang,² Jonathan Burnett,² Nick Ridler,² Chong Li,¹ and Martin Weides¹

¹*James Watt School of Engineering, University of Glasgow, Glasgow G12 8QQ, United Kingdom*

²*National Physical Laboratory, Hampton Road, Teddington TW11 0LW, United Kingdom*

(Dated: June 4, 2022)

Electromagnetic filtering is essential for the coherent control, operation and readout of superconducting quantum circuits at milliKelvin temperatures. The suppression of spurious modes around the transition frequencies of a few GHz is well understood and mainly achieved by on-chip and package considerations. Noise photons of higher frequencies – beyond the pair-breaking energies – cause decoherence, and require spectral engineering before reaching the packaged quantum chip. The external wires through the refrigerator down to the quantum circuit provides a direct path, and this article contains quantitative analysis and experimental data for noise photon flux through the coaxial filtered wiring. The coaxial cable room temperature attenuation and the noise photon flux estimates for typical wiring configurations are provided, and compact cryogenic microwave low-pass filters with CR-110 and Esorb-230 absorptive dielectric fillings along with experimental data at room and cryogenic temperatures and up to 70 GHz presented. The filter cut-off frequencies between 1 to 10 GHz are set by the filter length, and the roll-off is material dependent. The relative dielectric permittivity and magnetic permeability for the Esorb-230 material in the pair-breaking frequency range from 75 to 110 GHz are measured, and the filter properties in this frequency range are calculated. The filter contribution to the noise photon flux implies a dramatic reduction, proving their usefulness for experiments with superconducting quantum systems.

I. INTRODUCTION

Superconducting quantum circuits are a matured and salient experimental platform for the development of quantum technologies [1]. They are at the core of technological transition period to a so-called Noisy Intermediate-Scale Quantum (NISQ) level [2] where they are used for the construction of multi-qubit processors for quantum computation [3] and for creation of structures working as quantum simulators of other physical systems hard to study in a laboratory [4, 5]. They also find applications in sensing of amplitude, frequency [6, 7] and power [8] of microwave signals and in quantum metrology [9, 10]. For all of these tasks a quantum circuit needs to be well protected from external sources of decoherence while also, precise control of the quantum state of the circuit and fast readout are required. Rapid control is performed by quickly changing signals delivered to the quantum structure via coaxial wiring lines. In addition, these coaxial lines (for drive, flux control and readout [11]) bring electromagnetic noise to the structure and create additional channels of decoherence. The spectrum of noise can cover a wide range of frequencies, but control and readout are implemented within quite narrow frequency bands. Therefore, microwave attenuation, filtering and shielding are essential and inherent techniques used in the experiments with superconducting quantum circuits. In these experiments a superconducting circuit is placed at ~ 10 mK temperature of a cryogenic refrigerator, shielded from stray magnetic fields and thermal

radiation. Coaxial wiring for control and readout is thermally anchored at all temperature stages and attenuated and filtered at some of them. After interrogating the circuit, readout signals are amplified and also filtered.

Impinging radiation with frequencies outside the central and readout signals are detrimental to the quantum state and needs to be filtered. Quite often low-pass filters with GHz cut-off frequencies show higher transmissions towards infrared frequencies [12]. Radiation with frequencies $h\nu > 2\Delta$ breaks Cooper pairs, and hereby generates in the bulk of the circuit electrodes quasiparticles detrimental for the coherence of quantum states. Moreover, the mechanism of qubit decoherence associated with the photon-assisted electron tunnelling through a Josephson junction was also identified [13]. For Aluminium with superconducting energy gap $\Delta \simeq 170 \mu\text{eV}$ for film thickness ~ 100 nm [14] this corresponds to frequencies $\nu > 82$ GHz. In addition, it was shown that thermal radiation can generate fluctuations in the residual photon number and dephase superconducting qubits due to the ac Stark effect [15] and that the nonthermal populations of higher resonator modes are important for qubit dephasing [16].

There are two paths for the unwanted radiation to reach the circuit: direct impingement from higher temperature stages (free-space photons), and through TEM, TE and TM modes propagating in microwave coaxial wiring. It was demonstrated earlier [17, 18] that shielding of superconducting quantum circuits from infrared radiation is efficient to suppress the radiation flow through the first path. The infrared shielding improves quality factors of resonators and relaxation times of qubits. The control and readout signals reach the structure through

* sergey.danilin@glasgow.ac.uk

the second path, making the attenuation and filtering conditions more stringent. Here cryogenic attenuators are commonly used to lower the signal levels and reduce the number of thermal photons reaching the structure [11, 19, 20].

In our work we, first, provide a compact review of existing microwave filters (Sec. II) before calculating the attenuation of different microwave modes and estimating the flow of noise photons in a standard coaxial wire (Sec. III). We then (Sec. IV) demonstrate the design and manufacture of low-pass filters suitable for use in a cryogenic environment. In Sec. V, the microwave properties of filters are characterised at room temperature and ~ 3 K up to 70 GHz. Sec. VI provides the results of measurements of Esorb-230 material electromagnetic properties in the 75 to 110 GHz frequency range. Finally, the reduction of residual noise photon flux when the microwave filters are used is estimated in Sec. VII, which demonstrates their utility in experiments with superconducting quantum circuits and that Esorb-230 is suitable for the fabrication of infrared shields.

II. OVERVIEW ON CRYOGENIC MICROWAVE LOW-PASS FILTERS

Filters are used to limit the allowed frequency pass-band. In the following, we provide a short overview on cryogenic microwave low-pass filters that were developed to date. The most common and widely used type is metal powder filter in many different modifications: original copper and stainless steel powder [21, 22], based on silver epoxy [23], 50 Ω -matched bronze and stainless steel powder [24] and stripline embedded in magnetically-loaded Eccosorb dielectric [25], with built-in capacitive shunts to lower the cut-off frequency [26], based on printed circuit board (PCB) embedded in metal powder [27]. The other types are micro-fabricated miniature filters based on lossy coplanar transmission line [28] and on-chip filters for millimetre frequency range comprising arrays of SQUIDS or resistive capacitively shunted transmission lines [29]. Thin Thermocoax and stainless steel cables have filtering properties themselves and were tested as microwave cryogenic filters for experiments with quantum circuits [30, 31]. Different types of microwave filters are compared in reviews Ref. [32] and Ref. [33], the last one also introduces a transmission line ferrite compound filter. Most of these filters are tested experimentally at sub-GHz frequencies up to 20 GHz and only metal powder filters reported in Ref. [32] were measured up to 50 GHz which is still lower than the frequency corresponding to the aluminium superconducting energy gap. Both the lack of literature on filter transmission above 20 GHz and the superconducting circuit's sensitivity to stray radiation particular at these frequencies are addressed in the following sections.

III. NOISE PHOTON FLUX ESTIMATE

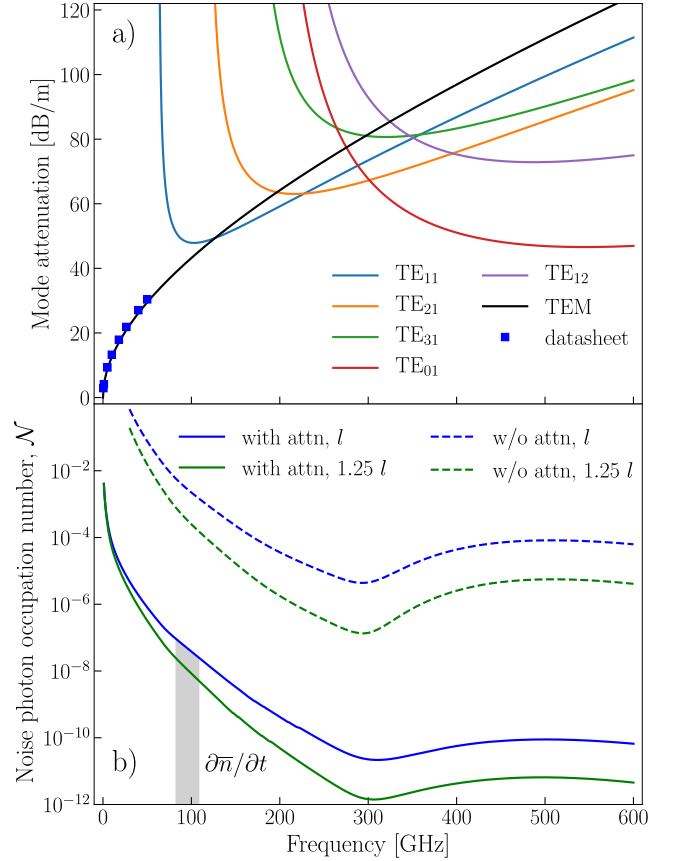


FIG. 1. (a) Room temperature attenuation caused by conductor and dielectric losses in UT086SS-SS cable for six modes with the lowest attenuation. All TM modes have higher attenuation. Blue squares show the data from Ref. [34] for TEM mode. (b) Estimate of the noise photon occupation number at the mixing chamber stage and for a single coaxial cable without filtering computed as a sum of contributions caused by each of the modes: for attenuators (assuming a constant attenuation over the entire frequency range) and two different lengths of coaxial line – two lower lines, without attenuators – two higher lines. Here an ideal thermalization of coaxial line and attenuators is assumed. Shaded area denotes the average number of noise photons ($\partial\bar{n}/\partial t = \int N d\nu$) exiting the coaxial line per second at the mixing chamber in the 82 to 110 GHz frequency range. See the Supplementary for the details of calculation.

Fig. 1(a) shows room temperature attenuation of five microwave TE modes with the lowest attenuation and TEM mode for UT086SS-SS stainless steel coaxial cable with PTFE dielectric including conductor and dielectric losses (see the Supplementary material). The range up to 600 GHz is chosen to include the global minimum ~ 47 dB/m of attenuation for TE modes at ~ 545 GHz where the number of noise photons transmitted through the line reaches a local maximum and then decreases due to the increased attenuation for higher frequencies. TM

modes all have much higher attenuation with the minimum of ~ 100 dB/m and can not noticeably contribute to the transmission of radiation. Higher order TE modes have attenuations ~ 50 dB higher than the minimal attenuation in this frequency range and their contribution to the transmission is negligible (less than 0.5%). We developed the model including frequency dependent attenuations, a significant improvement over past work [11] and required to compute the residual photon population (see the Supplementary). We estimate the noise photon occupation numbers $\mathcal{N}(x, \omega) = \partial^2 \bar{n} / \partial \nu \partial t$ – average number of photons passing through cross-section of the cable per unit bandwidth in a second – at the mixing chamber stage (Fig. 1(b)) by solving the equation

$$\frac{\partial \mathcal{N}(x, \omega)}{\partial x} = \frac{\alpha(\omega) \ln 10}{10} \left(n_{BE}(\omega, T(x)) - \mathcal{N}(x, \omega) \right) \quad (1)$$

consecutively for the coaxial line sections connecting the temperature stages of the refrigerator. Values of temperatures of refrigerator stages, lengths of coaxial cables between the stages, and arrangement of attenuators at the stages are given in the Supplementary. At those temperature stages where attenuators are placed, the function $\mathcal{N}(x, \omega)$ has abrupt changes described by the equation

$$\mathcal{N}(x, \omega)_{\text{out}} = \frac{\mathcal{N}(x, \omega)_{\text{in}}}{A} + \frac{A-1}{A} n_{BE}(\omega, T(x)). \quad (2)$$

In the equations above $n_{BE}(\omega, T(x))$ is the Bose-Einstein distribution at frequency ω and temperature $T(x)$, $A = 10^{a[\text{dB}]/10}$ is the attenuator attenuation, and $\alpha(\omega)$ is the room temperature attenuation constant. The attenuator scattering properties above 18 GHz are not provided by the manufacturers, thus we provide two estimates for i) the case when the attenuators work up to 600 GHz as well as they do up to 18 GHz, and ii) the case when the attenuators do not work at all and we can consider only cable attenuation. The average flow of noise photons in the frequency range from 82 GHz up to 110 GHz (all above the Cooper pair breaking energy for aluminum) without the use of infrared filters accounts for about $\partial \bar{n} / \partial t \sim 1420$ photons a second with attenuators (~ 85 million photons a second without attenuators). Extending the frequency range up to 600 GHz enlarges the noise photon flow by 35% (56%). Increasing the length of coaxial cables between each pair of refrigerator stages by 25% lowers the average flow of noise photons to ~ 335 (~ 10 million). The modest change in length by 25% has significant impact by more than a factor 4 in the noise photon flux which elucidates the strong dependence of the pair breaking photon flux without additional infrared filtering on the individual coaxial wiring within the cryostat. Lines in the Fig. 1(b) represent the lower bounds on the noise photon occupation numbers as the modes attenuation is reduced for lower temperature and this temperature dependence is not taken into account. As a note, thinner coaxial cables, such as UT047SS-SS and UT034SS-SS,

have higher attenuation per meter which leads to reduction of the noise photon flux, see Fig. 7 and the Supplementary.

IV. FILTER MATERIALS AND DESIGN

The microwave filters consist of two microwave connectors in a hollow Copper block with their PTFE removed. The centre conductor ends are soldered together, and the filter material is casted around the centre pins. This modified design from Ref. [35] is filled with two absorptive materials: CR-110 [36] and Esorb-230 [37]. Both materials are commercially available and easy to handle. These materials are magnetically-loaded epoxy absorbers which consist of a mixture of a low dielectric loss matrix with micrometer-scale magnetic particles, that produce a high loss tangent [38]. Together with a curing agent, it forms a rigid material that can be cast to fit around the central conductor and acts as a filter device. Absorption properties of these two materials are distinct not only due to the choice of dielectric material used, but more importantly because of the difference in density of magnetic particles in each mixture.

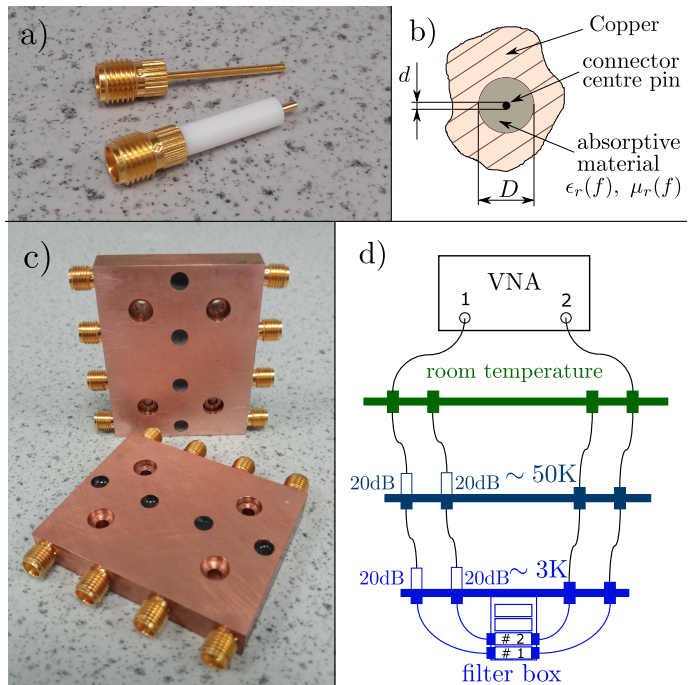


FIG. 2. a) Real image of SMA connectors used for the fabrication of filters. b) Schematic view of a cross-section of the filter. c) Real image of microwave filters tested in the work. d) Diagram of the setup used in cryogenic measurements of scattering parameters.

The filter is made by drilling a channel of diameter D in a Copper block (Fig. 2(b),(c)), two SMA connectors (Johnson 142-1721-051, knurl mount, Fig. 2(a)) are plugged in the channel from both sides so that the centre

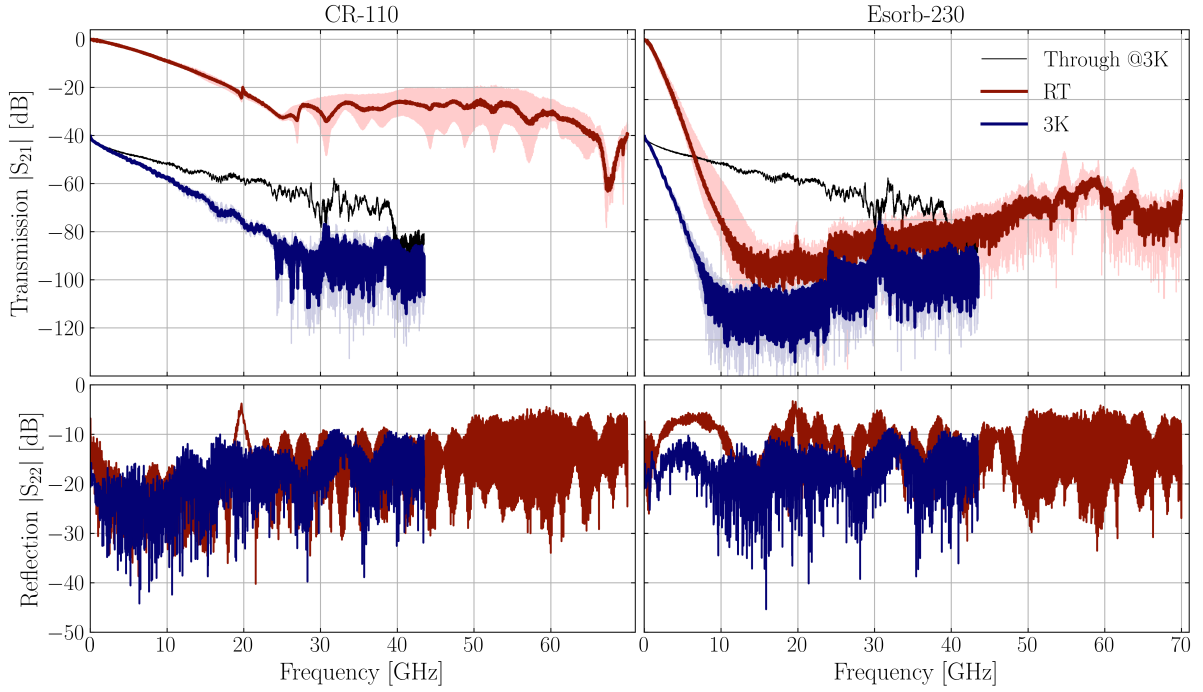


FIG. 3. Reflection $|S_{22}|$ and Transmission $|S_{21}|$ probed for CR-110 and Esorb-230 filters. Characteristics were obtained for room temperature and ~ 3 K (red and blue curves, respectively), where, for the latter, an extra 40 dB of attenuation was added to the incoming signal. Solid lines represent the average values for 4 filters measured at room temperature and 2 filters measured cryogenically. The RT data is already corrected by the calibration with 'through' connection. The light shaded areas represent the biggest deviation from the average among 4 or 2 filters correspondingly demonstrating reproducibility of manufacturing.

conductors are met at the middle of the channel and can be soldered together. The dielectric layer (PTFE) around the centre conductor is removed before the installation.

Finally, the volume between the centre conductor and the walls of channel is filled with either CR-110 or Esorb-230 absorptive material through the hole in the Copper enclosure at the middle of the channel. The same hole is used before to solder the ends of centre conductors.

For coaxial geometry of the filter characteristic impedance can be computed as [35]

$$Z(f) = \frac{Z_{\text{vac}} \ln(D/d)}{2\pi} \sqrt{\frac{\mu_r(f)}{\epsilon_r(f)}}, \quad (3)$$

here $Z_{\text{vac}} = \sqrt{\mu_0/\epsilon_0} \simeq 377\Omega$ is the impedance of free space, D is the diameter of the channel in Copper, d is the diameter of centre pin of the connector, $\mu_r(f) = \mu'(f) - j\mu''(f)$ and $\epsilon_r(f) = \epsilon'(f) - j\epsilon''(f)$ are relative magnetic permeability and electric permittivity of absorptive material. These material constants, and hence the optimal diameter D , depend on the frequency f [36]. Using the centre pin diameter $d = 1.27$ mm of the connectors we find the outer diameter $D^* = 5.3$ mm which minimises reflection $|S_{11}| = 20 \log_{10} |(Z - 50\Omega)/(Z + 50\Omega)|$ averaged in 1 to 18 GHz frequency range. The actual diameter $D = 5.1$ mm used in the manufacture, and given by the size of knurled part of the connectors, is very close to the optimal value D^* . It gives -31 dB average reflection

in the same frequency range with a maximum impedance deviation from 50Ω by 11Ω at 1 GHz.

V. SCATTERING PARAMETERS AT ROOM AND CRYOGENIC TEMPERATURES

All filters were initially characterised at room temperature using an Agilent Technologies E8361A vector network analyzer (VNA) to measure scattering parameters up to 70 GHz. Since the SMA connectors that are fitted to these filters are only specified to 18 GHz, measurements made above this frequency should be treated with care. This is because there is a likelihood that modes other than TEM modes will also be propagating. Afterwards, the same filters were tested at cryogenic temperatures inside a 3K refrigerator (see Fig. 2(d)). Rohde & Schwarz ZVA 40 VNA (measuring up to 43 GHz) was used for cryogenic measurements, and two 20 dB attenuators were placed at 50K and 4K temperature stages on the input line of the setup between the VNA port 1 and the filter box. For both cases, we measured "through" connections to later account for the attenuation of the wiring.

Reflection S_{22} and transmission S_{21} were probed and the resulting data was processed to exclude the frequency-dependant behaviour of the wiring. Results are shown in Fig. 3 for CR-110 and Esorb-230 filters at

	Attenuation [dB/cm]							
	1 GHz		3 GHz		5 GHz		8.6 GHz	
	RT	3 K	RT	3 K	RT	3 K	RT	3 K
CR-110	0.155	0.045	0.550	0.337	1.034	0.662	2.070	1.553
CR-110 [datasheet]	0.09	-	0.26	-	-	-	2.0	-
Esorb-230	1.053	0.740	4.980	4.269	9.623	7.772	18.433	14.611

TABLE I. Attenuation per unit length for CR-110 and Esorb-230 filters.

both temperatures. Since each box contains four filters (only two were probed at 3 K), we averaged their spectra, and the light shaded regions in the figure corresponds to the maximum deviation from this average. Both materials are characterized by a different -3dB point and roll-off slope in transmission. For CR-110, the transmitted signal amplitude decreases slower than for Esorb-230 and reaches about -35 dB at 25 GHz. For Esorb-230, the amplitude reaches the noise floor of the instrument at ~ 15 GHz for room temperature measurement, and the filter transmission is covered by noise floor for higher frequencies, see the datasheet [39]. The difference in noise floor is a consequence of using two distinct VNAs. The small peak seen for CR-110 at room temperature around 20 GHz is a feature caused by a small resonance of the cable used.

For reflection data, there is a slightly higher amplitude for Esorb-230 which is a result of designing the filters using the specifications of CR-110 (data for $\epsilon_r(f)$ and $\mu_r(f)$ was not available for the former). Impedance of Esorb-230 filters was not matched to 50Ω as this is a newer, less common material which parameters were not known *a priori*. As a result, the signal reflection was not minimized at the filter design stage.

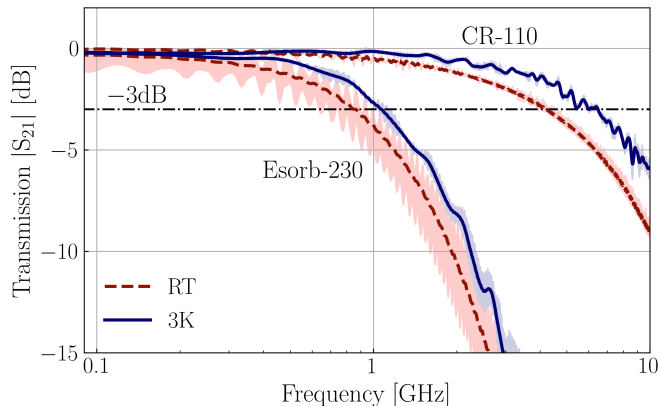


FIG. 4. Low frequency behaviour of filters. -3 dB cut-off frequencies are distinct for both materials and increase when filters are cooled down to 3K.

The difference in -3 dB point is even more evident when we zoom in at low frequencies, as seen in Fig. 4. The transmission data indicates a shift in -3 dB points to higher frequencies as the temperature is lowered to

cryogenic regime (blue curves). The shift is approximately 50% for CR-110 and 30% for Esorb-230 and can be accounted for an increase in conductivity of metallic particles as it is usually the case for metal powder filters [22, 24]. The characteristics of filters are summarised in the tables I and II.

	-3dB point [GHz]			Atten. @ 5GHz [dB]	
	RT	3 K	δf_{-3dB}	RT	3 K
CR-110	4.23	6.30	48.9 %	3.7	2.4
Esorb-230	0.83	1.07	28.9 %	34.6	28.0

TABLE II. -3 dB frequency points of filters (CR-110 and Esorb-230) and the filters attenuation at 5 GHz for room and cryogenic temperature.

VI. ESORB-230 CHARACTERISTICS IN EXTREMELY HIGH FREQUENCY BAND

To study absorption properties of the Esorb-230 material used for the filters at frequencies above the superconducting gap of Aluminium, we measured S_{11} and S_{21} parameters of waveguide sections filled with the material. WR10 rectangular waveguides $2.54 \text{ mm} \times 1.27 \text{ mm}$ were used in the measurements, see Fig. 5(a). Two sections of waveguides with 2.0 mm and 2.7 mm thicknesses were tested in the 75 to 110 GHz frequency range. Results of the S-parameter measurements are shown in the Fig. 5(b).

The setup is calibrated to measure the scattering parameters with respect to the reference planes at the facets of the waveguide spacers, and we can determine the relative permittivity $\epsilon_r(f)$ and permeability $\mu_r(f)$ of the Esorb-230 material using the Nicolson-Ross-Weir (NRW) method [40]. The method has ambiguity related to *a priori* unknown branch of the complex logarithm function enumerated by the index n and resulting in a set of solutions. This ambiguity is resolved by having two sets of data obtained for two thicknesses of the waveguide sections (see the Supplementary). We determine the electromagnetic parameters (ϵ' , μ' , $\tan(\delta)$, $\tan(\delta_m)$) for each section thickness and each branch n and simulate the S-parameters with Ansys HFSS (High-Frequency Structure Simulator) for the experimental setting. We check the obtained electromagnetic parameters by comparing the

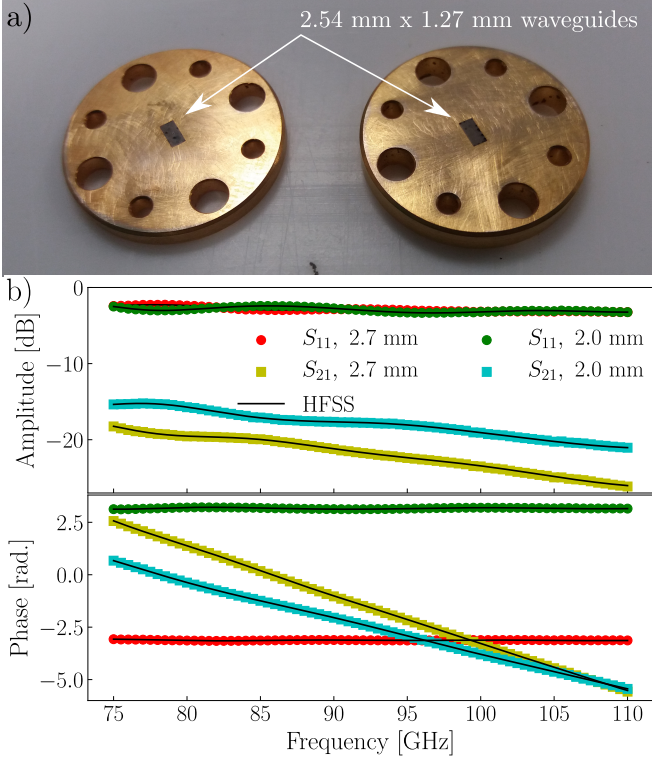


FIG. 5. a) Rectangular WR10 2.54 mm \times 1.27 mm waveguide sections filled with the Esorb-230 material. The spacers are used for the S_{11} and S_{21} parameters measurement in the 75 to 110 GHz frequency range to determine the electromagnetic properties (ϵ_r, μ_r) of the material. b) Amplitude and phase of scattering parameters measured for both waveguide spacers. The solid black lines show the results of HFSS simulation with electromagnetic parameters extracted by the NRW method.

simulated S-parameters with the measured ones and find a good agreement between them (Fig. 5(b)). The $\epsilon'(f)$ and $\mu'(f)$ found for $d = 2$ mm thickness and branch $n = 2$ and $d = 2.7$ mm and $n = 3$ coincide well (see the Supplementary), and we determine all electromagnetic parameters as the mean values of these two branches plotted in Fig. 6.

VII. RESIDUAL NOISE PHOTONS

We estimate the reduction in noise photon occupation number caused by the addition of the Esorb-230 filters at the mixing chamber plate of a dilution refrigerator. The number of photons reaching the filter input is described by the noise photon occupation number function computed earlier for the case with attenuators and length l of the coaxial wiring (Fig. 1(b), blue line). For the frequency range up to 70 GHz, where the filters were directly tested, we employ the measured S_{21} parameters to estimate the upper bound of the number of photons transmitted through the filter. The filter attenuation

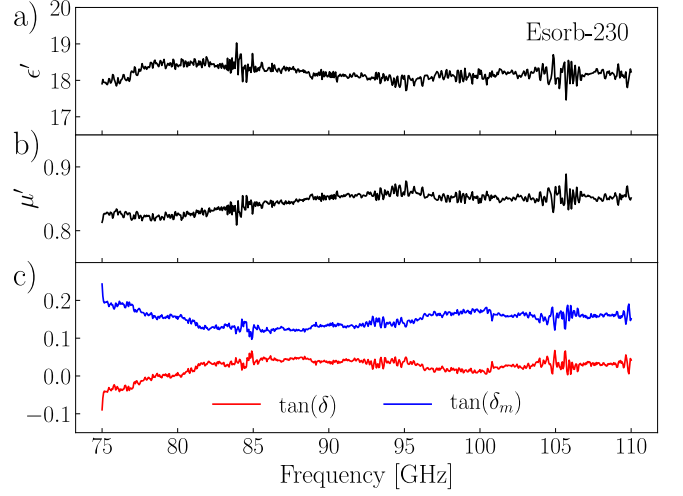


FIG. 6. Electromagnetic parameters of the Esorb-230 material in the frequency range from 75 to 110 GHz. (a) Real part of the relative dielectric permittivity. (b) Real part of the relative magnetic permeability. (c) Dielectric and magnetic loss tangents.

$A(f) = P_{\text{in}}(f)/P_{\text{out}}(f)$ is

$$A = 10^{-\frac{\overline{S_{21}}}{10}}, \quad \overline{S_{21}} = \left(\frac{1}{4} \sum_{i=1}^4 (S_{21})_i \right) - (S_{21})_{\text{thru}}. \quad (4)$$

$\overline{S_{21}}$ is the mean value of transmission coefficient over four measured filters. The attenuation caused by the wiring is excluded by subtracting the transmission measured for the "through" connection $(S_{21})_{\text{thru}}$.

Using the filter attenuation Eq. (4) and the Eq. (2), we compute the upper bound of the noise photon occupation number after the filter up to 70 GHz (Fig. 7, black line).

In the frequency range from 75 to 110 GHz, only the TEM and TE_{11} modes are supported by the UT086SS-SS coaxial cable. Due to the reflection, the number of photons entering the filter per second \mathcal{N}_2 is lower than the number of photons reaching the filter input per second \mathcal{N}_1 . This can be expressed as

$$\mathcal{N}_2 = \mathcal{N}_1 \left(1 - \left| \frac{Z_2 - Z_1}{Z_2 + Z_1} \right|^2 \right). \quad (5)$$

For TEM mode, Z_1 and Z_2 are the characteristic impedances of the coaxial line and the filter correspondingly Eq. (3). For TE_{11} mode, the characteristic impedance is not defined, and we use instead the wave impedances $Z_w(\omega)$ determined as

$$Z_w(\omega) = \frac{\omega \mu_0 \mu_r(\omega)}{\sqrt{\frac{\omega^2}{c^2} \epsilon_r(\omega) \mu_r(\omega) - k_c^2}}. \quad (6)$$

Here, ϵ_r and μ_r are the relative dielectric permittivity and magnetic permeability of the PTFE or Esorb material, and k_c is the TE_{11} mode critical wave-vector for the coaxial line or the filter.

Next, we compute the attenuation constants related to the conductor losses α_c [dB/m] and the dielectric and magnetic losses α_{dm} [dB/m] for both modes in the filter (see the Supplementary). Loss tangents of the Esorb-230 material are not small, and we compare the attenuation constants computed without simplifications conditioned by the smallness of losses and using the simplified expressions as it was done for coaxial lines. We find only a small difference between the two ways. The losses in the conductors of the filter can be neglected as they are about three orders of magnitude smaller than the dielectric and magnetic losses in the Esorb-230 material. The total filter attenuation then reads

$$A(f) = 10^{-\frac{\alpha_{dm}(f)l}{10}}, \quad (7)$$

where $l = 35.8$ mm is the length of the filter. This accounts for ~ 237 dB at 100 GHz frequency for both modes. We use this frequency dependent attenuation Eq. (7) and the number of photons entering the filter a second \mathcal{N}_2 for each of the two modes in the Eq. (2) to get the number of noise photons transmitted through the filter per second. By summing up the results for two modes, we find an estimate for the noise photon occupation number \mathcal{N} [Hz $^{-1}$ s $^{-1}$] transmitted through the filter in the frequency range from 75 to 110 GHz (Fig. 7, blue line).

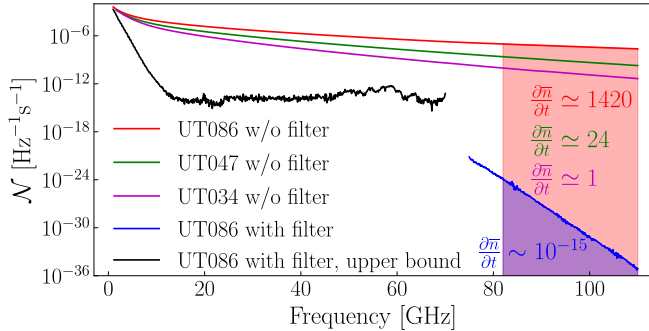


FIG. 7. The estimation of reduction of noise photon occupation number caused by the use of the Esorb-230 filter or thinner UT047SS-SS and UT034SS-SS coaxial cables. Red line shows the case of unfiltered UT086SS-SS coaxial line, where on average $\partial\bar{n}/\partial t \simeq 1420$ photons exit per second the coaxial cable end at the mixing chamber in the frequency range from 82 to 110 GHz. When thinner cables are used the average photon number is reduced (green and magenta lines). The use of the filter dramatically reduces the average flow of noise photons ($\partial\bar{n}/\partial t \ll 1$) for the same frequency range. Blue line is an estimate based on the measured electromagnetic properties of Esorb-230, and the black line is the upper bound estimated based on the measured S-parameters of the filter.

The estimates of noise photon occupation number at the mixing chamber stage for thinner cables (UT047SS-SS and UT034SS-SS) of the same length and without the filter are shown for comparison in Fig. 7 (green and magenta line). In these cases, the average number of noise photons reaching per second an experimental structure at

milliKelvin temperature is reduced in the 82 to 110 GHz range above the superconducting energy gap of the Aluminium. The use of the Esorb-230 filters is expected to reduce the number of noise photons much more dramatically for the same frequency range, to values $\partial\bar{n}/\partial t \ll 1$. Despite the wiring with thinner and longer cables has an advantage in the noise photon flux, it can not reduce the noise photon flux to the low values possible to achieve with the Esorb-230 filters. Moreover, the thinner the cable, the stronger the dependence of attenuation on frequency which makes the transmission steeper in the operational frequency band below 20 GHz. Though the estimates are made based on the room temperature measurements, the transmission properties of the filters will not change much at the cryogenic temperatures as it can be seen in the Fig. 3 and Fig. 4.

VIII. CONCLUSIONS

The article provides an estimate of the spectral density of noise photons reaching an experimental structure at milliKelvin temperature per second through a coaxial line in the frequency range up to 600 GHz. This elucidates the necessity of microwave to infrared filtering of coaxial wiring for experiments with quantum systems. The estimation is done for a dilution refrigerator wiring configuration typical for the experiments with superconducting quantum circuits and UT085SS-SS, UT047SS-SS, and UT034SS-SS types of cables. Cryogenic microwave frequency filters based on the CR-110 and Esorb-230 absorptive materials are manufactured. Transmission and reflection properties of the filters are tested up to 43 GHz cryogenically and up to 70 GHz at room temperature. Electromagnetic properties of the Esorb-230 material are separately measured in the frequency range from 75 to 110 GHz covering a range of frequencies above the superconducting gap of Aluminium. Based on the measurements, the residual number of photons reaching a sample structure at milliKelvin temperature per second is estimated when the filters are used. The results will allow for coaxial wiring and filter solutions to reduce the impact of noise photons of higher frequencies including the pair breaking energies of metallic superconductors.

IX. ACKNOWLEDGEMENT

The authors are thankful for the support from the European Research Council (ERC) under the Grant Agreement No. 648011, the Engineering and Physical Sciences Research Council (EPSRC) under the Grant Agreements No. EP/T018984/1 and No. EP/T001062/1, the Scottish Research Partnership in Engineering (SRPe) under the Grant Agreement NMIS-IDP/025 and Seeqc UK LIMITED for a studentship (JB).

-
- [1] P. Krantz et al. A quantum engineer's guide to superconducting qubits. *Appl. Phys. Rev.*, 6(021318), 2019.
- [2] J. Preskill. Quantum computing in NISQ era and beyond. *Quantum*, 2(79), 2018.
- [3] F. Arute et al. Quantum supremacy using a programmable superconducting processor. *Nature*, 574:505–510, 2019.
- [4] A.A. Houck, H.E. Türeci, and J. Koch. On-chip quantum simulation with superconducting circuits. *Nature Physics*, 8:292–299, 2012.
- [5] Y. Yanay et al. Realizing the two-dimensional hard core Bose-Hubbard model with superconducting qubits. *ArXiv:1910.00933v1*, 2019.
- [6] A. Schneider et al. Local sensing with the multilevel ac Stark effect. *Phys. Rev. A*, 97(062334), 2018.
- [7] M. Kristen, A. Schneider, A. Stehli, et al. Amplitude and frequency sensing of microwave fields with a superconducting transmon qubit. *npj Quantum Inf.*, 6(57), 2020.
- [8] T. Hönigl-Decrinis et al. Two-level system as a quantum sensor for absolute calibration of power. *Phys. Rev. Applied*, 13(024066), 2020.
- [9] S. Danilin et al. Quantum-enhanced magnetometry by phase estimation algorithms with a single artificial atom. *npj Quantum Information*, 4(29), 2018.
- [10] M. Bal et al. Ultrasensitive magnetic field detection using a single artificial atom. *Nat Commun*, 3(1324), 2012.
- [11] S. Krinner et al. Engineering cryogenic setups for 100-qubit scale superconducting circuit systems. *EPJ Quantum Technology*, 6(2), 2019.
- [12] www.minicircuits.com. *See the datasheets for models VLF-5850+, VLF-2850+, VLF-2350+.*
- [13] M. Houzet et al. Photon-assisted charge-parity jumps in a superconducting qubit. *Phys. Rev. Lett.*, 123(107704), 2019.
- [14] D. H. Douglass and R. Meservey. Energy gap measurements by tunneling between superconducting films. i.temperature dependence. *Phys. Rev.*, 135(A19), 1964.
- [15] F. Yan et al. Distinguishing coherent and thermal photon noise in a circuit quantum electrodynamical system. *Phys. Rev. Lett.*, 120(260504), 2018.
- [16] A.P. Sears et al. Photon shot noise dephasing in the strong-dispersive limit of circuit QED. *Phys. Rev. B*, 86(180504(R)), 2012.
- [17] R. Barends et al. Minimizing quasiparticle generation from stray infrared light in superconducting quantum circuits. *Appl. Phys. Lett.*, 99(113507), 2011.
- [18] A.D. Córcoles et al. Protecting superconducting qubits from radiation. *Appl. Phys. Lett.*, 99(181906), 2011.
- [19] J. H. Yeh et al. Microwave attenuators for use with quantum devices below 100 mk. *J. Appl. Phys.*, 121(224501), 2017.
- [20] J. H. Yeh et al. Hot electron heatsinks for microwave attenuators below 100 mk. *Appl. Phys. Lett.*, 114(152602), 2019.
- [21] J.M. Martinis, M.H. Devoret, and J. Clarke. Experimental tests for the quantum behaviour of a macroscopic degree of freedom: The phase difference across a josephson junction. *Phys. Rev. B*, 35(10), 1987.
- [22] A. Fukushima et al. Attenuation of microwave filters for single-electron tunneling experiments. *IEEE Transactions on Instrumentation and Measurement*, 46(2), 1997.
- [23] C.P. Scheller et al. Silver-epoxy microwave filters and thermalizers for millikelvin experiments. *Appl. Phys. Lett.*, 104(211106), 2014.
- [24] F.P. Milliken et al. 50 Ω characteristic impedance low-pass metal powder filters. *Rev. Sci. Instrum.*, 78(024701), 2007.
- [25] D. F. Santavicca and D. E. Prober. Impedance-matched low-pass stripline filters. *Meas.Sci. Technol.*, 19(087001), 2008.
- [26] A. Lukashenko and A.V. Ustinov. Improved powder filters for qubit measurements. *Rev. Sci. Instrum.*, 79(014701), 2008.
- [27] F. Mueller et al. Printed circuit board metal powder filters for low electron temperatures. *Rev. Sci. Instrum.*, 84(044706), 2013.
- [28] D. Vion et al. Miniature electrical filters for single electron devices. *Journal of Applied Physics*, 77(2519), 1995.
- [29] J.S. Lehtinen et al. Characterizing superconducting filters using residual microwave background. *Supercond. Sci. Technol.*, 30(055006), 2017.
- [30] A.B. Zorin. The thermocoax cable as the microwave frequency filter for single electron circuits. *Review of Scientific Instruments*, 66(4296), 1995.
- [31] G. Tancredi, S. Schmidlin, and P.J. Meeson. Note: cryogenic coaxial microwave filters. *Rev. Sci. Instrum.*, 85(026104), 2014.
- [32] K. Bladh et al. Comparison of cryogenic filters for use in single electronics experiments. *Rev. Sci. Instrum.*, 74(1323), 2003.
- [33] M. Thalmann et al. Comparison of cryogenic low-pass filters. *Rev. Sci. Instrum.*, 88(114703), 2017.
- [34] Micro-Coax. Catalogue: Microwave & RF cable. page 30, July 2015.
- [35] M. Fang. Development of hardware for scaling up superconducting qubits and simulation of quantum chaos. *Bachelor's Honors Thesis, UCSB*, 2015.
- [36] www.laird.com. Eccosorb MF. page 3, 2018.
- [37] Electronic Service GmbH. *Esorb-LE : Magnetically Loaded Epoxy Absorber*.
- [38] I. Zivkovic and A. Murk. Characterization of magnetically loaded microwave absorbers. *Progress In Electromagnetics Research*, 33:277–289, 2011.
- [39] https://www.keysight.com/gb/en/assets/7018-08817/data-sheets-archived/5988_7988.pdf. Agilent PNA Microwave Network Analyzers.
- [40] E.J. Rothwell et al. Analysis of the nicolson-ross-weir method for characterizing the electromagnetic properties of engineered materials. *Progress In Electromagnetics Research*, 157:31–47, 2016.

Supplementary material for “Engineering the microwave to infrared noise photon flux for superconducting quantum systems”

Sergey Danilin,^{1,*} João Barbosa,¹ Michael Farage,¹ Zimo Zhao,¹ Xiaobang Shang,² Jonathan Burnett,² Nick Ridler,² Chong Li,¹ and Martin Weides¹

¹*James Watt School of Engineering, University of Glasgow, Glasgow G12 8QQ, United Kingdom*

²*National Physical Laboratory, Hampton Road, Teddington TW11 0LW, United Kingdom*

I. AVERAGE FLOW OF NOISE PHOTONS

To compute the noise photon occupation number $\mathcal{N} = \partial^2 \bar{n} / \partial \nu \partial t$ – average number of noise photons in a unit bandwidth crossing a cross-section of microwave wiring line in a second – we consider sections of coaxial line installed between the temperature stages of a dilution refrigerator and going from room temperature down to the mixing chamber plate. We assume a perfect thermalization at the temperature stages so that in equilibrium the temperature reduces linearly from the hot end T_H to the cold end T_C ,

$$T(x) = -\frac{(T_H - T_C)}{L}x + T_H. \quad (1)$$

Here x denotes position from the hot end to the cold end, and L is the length of the coaxial line section connecting the two stages.

If the coaxial cable has attenuation per unit length $\alpha(\omega)$ [dB/m], a short section dx of the line will have attenuation αdx [dB] = $10 \log_{10} A$, where A is the ratio of powers at the input and the output of the section $A = P_{\text{in}}/P_{\text{out}}$. Noise photon occupation number at the input and the output of the section are related as

$$\mathcal{N}_{\text{out}} = \frac{\mathcal{N}_{\text{in}}}{A} + \frac{A-1}{A} n_{BE}(\omega, T(x)), \quad (2)$$

here $n_{BE}(\omega, T(x)) = 1/(\exp[\hbar\omega/k_B T(x)] - 1)$ is the Bose-Einstein distribution at frequency ω and temperature $T(x)$. Taking into account that dx is small we can express through α the ratio $A = 1 + \frac{\alpha dx}{10} \ln 10$ and write Eq.(2) as

$$\mathcal{N}(x) + d\mathcal{N} = \frac{\mathcal{N}(x)}{1 + \frac{\alpha dx}{10} \ln 10} + \frac{\frac{\alpha dx}{10} \ln 10}{1 + \frac{\alpha dx}{10} \ln 10} n_{BE}(\omega, T(x)). \quad (3)$$

Leaving only the terms up to the first-order in the small parameter $\alpha(\omega)dx$ we arrive at the first-order linear differential equation

$$\frac{d\mathcal{N}(x)}{dx} = \frac{\alpha(\omega) \ln 10}{10} \left(n_{BE}(\omega, T(x)) - \mathcal{N}(x) \right). \quad (4)$$

Once the temperature distribution Eq.(1) and the attenuation per unit length α are known, it is possible to solve this equation numerically and find the noise photon occupation number $\mathcal{N}(x)$ as a function of the position x along the coaxial line. The value $\mathcal{N}(0)$ here is known and serves as a boundary condition for the differential equation.

Starting from room temperature, where the boundary condition is $\mathcal{N}(0) = n_{BE}(\omega, T_{\text{RT}})$, we can compute the function $\mathcal{N}(x)$ for the frequency ω consecutively for each section of coaxial line down to the mixing chamber plate. For those stages where attenuators are installed, the function $\mathcal{N}(x)$ will reduce abruptly according to Eq.(2) with \mathcal{N}_{in} and \mathcal{N}_{out} being the function values before and after the attenuator and n_{BE} – the distribution corresponding to the temperature of the stage. The ratio $A = 10^{a[\text{dB}]/10}$ here will be given by the attenuator value a [dB]. To perform the computation, we have to know the temperatures of dilution refrigerator stages, the arrangement of attenuators at the temperature stages with their values, and lengths of coaxial line sections connecting each pair of stages.

We used in our computations the temperatures [300, 35, 2.85, 0.882, 0.082, 0.006] K for room temperature, “50K”, “4K”, “Still Chamber”, “Cold Plate”, and “Mixing Chamber” stage correspondingly. Lengths of coaxial line sections

* sergey.danilin@glasgow.ac.uk

were [228, 271, 263, 231, 306] mm for interconnects between two neighbour stages from the previous list, and the arrangement of attenuators was [0, 20, 0, 20, 20] dB meaning that 20 dB attenuators are installed at the "4K", "Cold Plate", and "Mixing Chamber" stages.

Integrating the function $\mathcal{N}(\omega, x_{\text{end}})$ at the "Mixing Chamber" stage in a desired frequency range we can find the average number of noise photons coming out of the end of the line for this frequency range in a second.

II. ATTENUATION CONSTANT FOR DIFFERENT ELECTROMAGNETIC MODES OF A COAXIAL LINE

We consider UT086SS-SS, UT047SS-SS, and UT034SS-SS coaxial lines with stainless steel inner and outer conductors, PTFE dielectric, and the following parameters: radius of the inner conductor $a = 0.255$ mm for UT086, $a = 0.1435$ mm for UT047, and $a = 0.1015$ mm for UT034 cable, inner radius of the outer conductor $b = 0.835$ mm for UT086, $b = 0.47$ mm for UT047, and $b = 0.33$ mm for UT034 cable, electrical conductivity of stainless steel conductors $\sigma = 1.41 \cdot 10^6$ S/m, relative dielectric constant of the PTFE dielectric $\epsilon' = \text{Re}(\epsilon_r) = 2.08$, relative permeability of PTFE $\mu' = \text{Re}(\mu_r) = 1$, and the PTFE tangent of dielectric losses $\tan \delta = 0.0004$.

The PTFE dielectric is not magnetic and there are only two types of energy losses – dielectric losses and losses in conductors. Energy flow through a cross section of a coaxial line at the position z along the line drops down as $P(z) = P_0 \exp(-2\alpha z)$, where α is attenuation constant and P_0 is the energy flow at the input of the line. In our case of non-magnetic materials we have $\alpha = \alpha_c + \alpha_d$ distinguishing the two types of energy losses. We use cylindrical coordinates $(\vec{\rho}, \vec{\phi}, \vec{z})$ with axis z along the coaxial line direction. Taking derivative of the above expression for the energy flow we get $-P_l(z) = dP(z)/dz = -2\alpha P(z)$. From here the attenuation constant can be expressed as

$$\alpha = \frac{P_l}{2P_0}. \quad (5)$$

P_0 here is the energy flow at zero position [W] and P_l is power dissipated per meter of line [W/m] at zero position.

The general expression to find P_0 is

$$P_0 = \frac{1}{2} \text{Re} \int_{\rho=a}^b \int_{\phi=0}^{2\pi} (\vec{E} \times \vec{H}^*)_z \rho d\phi d\rho = \frac{1}{2} \text{Re} \int_{\rho=a}^b \int_{\phi=0}^{2\pi} (E_\rho H_\phi^* - E_\phi H_\rho^*) \rho d\phi d\rho. \quad (6)$$

This expression is the integral of Umov-Poynting vector over the cross-sectional area of a coaxial line, and quantities under the integrals are electromagnetic field components.

Conductor losses per unit length can be found as

$$P_l = \frac{R_s}{2} \int_{C_1+C_2} \vec{H}_t \cdot \vec{H}_t dl = \frac{R_s}{2} \left[\int_0^{2\pi} (|H_z|^2 + |H_\phi|^2) a d\phi + \int_0^{2\pi} (|H_z|^2 + |H_\phi|^2) b d\phi \right]. \quad (7)$$

Here the integral is taken over the circumferences of conductors, values of fields are taken at $\rho = a$ and $\rho = b$ for the first and the second integrals correspondingly, and R_s is the surface resistance in $[\Omega]$.

The attenuation constant related to the dielectric losses for TE or TM mode reads

$$\alpha_d = \frac{k^2 \tan \delta}{2\beta} = \frac{k^2 \tan \delta}{2\sqrt{k^2 - k_c^2}}, \quad (8)$$

which is valid only if $k > k_c$. k_c is a critical wave-vector.

The major mode for any coaxial transmission line is **TEM mode** for which $E_z = H_z = 0$, and the cut-off frequency is zero ($k_c = 0$).

For TEM mode the attenuation constant $\alpha = \alpha_c + \alpha_d$ is equal to

$$\alpha_{\text{TEM}} = \frac{R_s}{4\pi Z_0} \left(\frac{1}{a} + \frac{1}{b} \right) + \frac{\pi \omega \epsilon_0 \epsilon' \tan \delta Z_0}{\ln(b/a)}. \quad (9)$$

Here $R_s = \sqrt{\frac{\omega \mu_0 \mu'}{2\sigma}}$ is the surface resistance in $[\Omega]$, and $Z_0 = \sqrt{\frac{\mu_0 \mu'}{\epsilon_0 \epsilon'}} \frac{\ln(b/a)}{2\pi}$ is the characteristic impedance of the coaxial line. The first term in the Eq. (9) represents the attenuation related to losses in the conductors and the second term – the attenuation related to the dielectric losses, this term also can be expressed as $\alpha_{d,\text{TEM}} = k \tan \delta / 2$. Attenuation constant in the Eqs. (5), (8), and (9) are in [Np/m] units (Neper per meter) and to convert it to [dB/m] one has to multiply the result by $20 \log_{10}(e)$, [dB/m] = $20 \log_{10}(e) \cdot [\text{Np/m}]$.

For **TE modes** there is no electric field component along the coaxial line $E_z = 0$, and the cut-off frequency has a non-zero value. In this case, $\beta = \sqrt{k^2 - k_c^2}$, where $k_c = 2\pi f_c \sqrt{\epsilon' \mu'} / c > 0$. All components of the field can be expressed through H_z which, in turn, can be found from the Helmholtz equation and has a general form of

$$H_z(\rho, \phi, z) = A \cos(n\phi) (C J_n(k_c \rho) + D Y_n(k_c \rho)) \exp(-j\beta z), \quad (10)$$

here $J_n(x)$ and $Y_n(x)$ are Bessel functions of the first and the second kind correspondingly. Satisfying the boundary conditions on tangential components of electric field at conductor surfaces $E_\phi(\rho = a) = E_\phi(\rho = b) = 0$ we arrive to the equation $J'_n(k_c a) Y'_n(k_c b) - J'_n(k_c b) Y'_n(k_c a) = 0$. The roots of the equation $k_c^{n,m}$, where index m denotes the m th root of the equation, are the cut-off wave-vectors determining the mode indexes TE_{nm} . Once critical wave vectors k_c are found we can write down all components of the field

$$\begin{aligned} E_\rho &= \frac{j\omega\mu_0\mu_r}{k_c^2\rho} A n \sin(n\phi) \left(J_n(k_c\rho) - \frac{J'_n(k_c b)}{Y'_n(k_c b)} Y_n(k_c\rho) \right) \exp(-j\beta z), \\ E_\phi &= \frac{j\omega\mu_0\mu_r}{k_c} A \cos(n\phi) \left(J'_n(k_c\rho) - \frac{J'_n(k_c b)}{Y'_n(k_c b)} Y'_n(k_c\rho) \right) \exp(-j\beta z), \\ H_\rho &= \frac{-j\beta}{k_c} A \cos(n\phi) \left(J'_n(k_c\rho) - \frac{J'_n(k_c b)}{Y'_n(k_c b)} Y'_n(k_c\rho) \right) \exp(-j\beta z), \\ H_\phi &= \frac{j\beta}{k_c^2\rho} A n \sin(n\phi) \left(J_n(k_c\rho) - \frac{J'_n(k_c b)}{Y'_n(k_c b)} Y_n(k_c\rho) \right) \exp(-j\beta z), \\ H_z &= A \cos(n\phi) \left(J_n(k_c\rho) - \frac{J'_n(k_c b)}{Y'_n(k_c b)} Y_n(k_c\rho) \right) \exp(-j\beta z). \end{aligned} \quad (11)$$

In these equations the constant A has units of [A/m].

Numerical calculations for UT086SS-SS, UT047SS-SS, and UT034SS-SS coaxial cables give us TE modes critical wave-vectors k_c and cut-off frequencies f_c . Six TE modes with the lowest cut-off frequencies are given in the Table I for these three types of coaxial cables.

	UT086SS-SS		UT047SS-SS		UT034SS-SS	
TE mode	k_c [1/m]	f_c [GHz]	k_c [1/m]	f_c [GHz]	k_c [1/m]	f_c [GHz]
11	1887	62.5	3352	111.0	4766	157.7
21	3549	117.5	6305	208.7	8972	297.0
31	5004	165.6	8889	294.3	12658	419.1
01	5673	187.8	10077	333.6	14392	476.5
12	6176	204.5	10971	363.2	15652	518.2
41	6362	210.6	11303	374.2	16097	532.9

TABLE I. Six TE modes of UT086SS-SS, UT047SS-SS and UT034SS-SS coaxial cables with the lowest cut-off frequencies.

We find for a TE mode with the use of expressions (11) according to the formulas (6) and (7)

$$\begin{aligned} P_0 &= \frac{\pi\omega\mu_0\mu_r Re\{\beta\} |A|^2}{2k_c^4} \int_{k_c a}^{k_c b} \left[\frac{n^2}{x} \left(J_n(x) - \frac{J'_n(k_c b)}{Y'_n(k_c b)} Y_n(x) \right)^2 + x \left(J'_n(x) - \frac{J'_n(k_c b)}{Y'_n(k_c b)} Y'_n(x) \right)^2 \right] dx, \quad \text{and} \\ P_l &= \frac{\pi |A|^2 R_s}{2} \left\{ a \left(1 + \frac{|\beta|^2 n^2}{k_c^4 a^2} \right) \left[J_n(k_c a) - \frac{J'_n(k_c b)}{Y'_n(k_c b)} Y_n(k_c a) \right]^2 + b \left(1 + \frac{|\beta|^2 n^2}{k_c^4 b^2} \right) \left[J_n(k_c b) - \frac{J'_n(k_c b)}{Y'_n(k_c b)} Y_n(k_c b) \right]^2 \right\}. \end{aligned} \quad (12)$$

These quantities can be computed numerically and we can get $\alpha_{c,TE}$ according to the Eq.(5). Attenuation constants related to the dielectric losses are computed according to the Eq. (8) for each mode with corresponding k_c value. Total attenuation per meter at room temperature for six TE modes with the lowest cut-off frequencies and TEM modes are shown in the Fig.1 for UT086SS-SS (a), UT047SS-SS (c), and UT034SS-SS (e) coaxial cable.

For **TM modes** there is no magnetic field component along the line $H_z = 0$. Modes of this type have also non-zero cut-off frequencies f_c . This time, all components of the field can be expressed through E_z component. E_z is a solution of the Helmholtz wave equation and has a general form which is the same as Eq.(10). Components E_z and E_ϕ have similar radial dependence which includes $(C J_n(k_c \rho) + D Y_n(k_c \rho))$. They both have to be zero at the surfaces of conductors to satisfy the boundary conditions which leads to the equation $J_n(k_c a) Y_n(k_c b) - J_n(k_c b) Y_n(k_c a) = 0$. Importantly, here the Bessel functions enter the equation but not their derivatives as it was for TE modes.

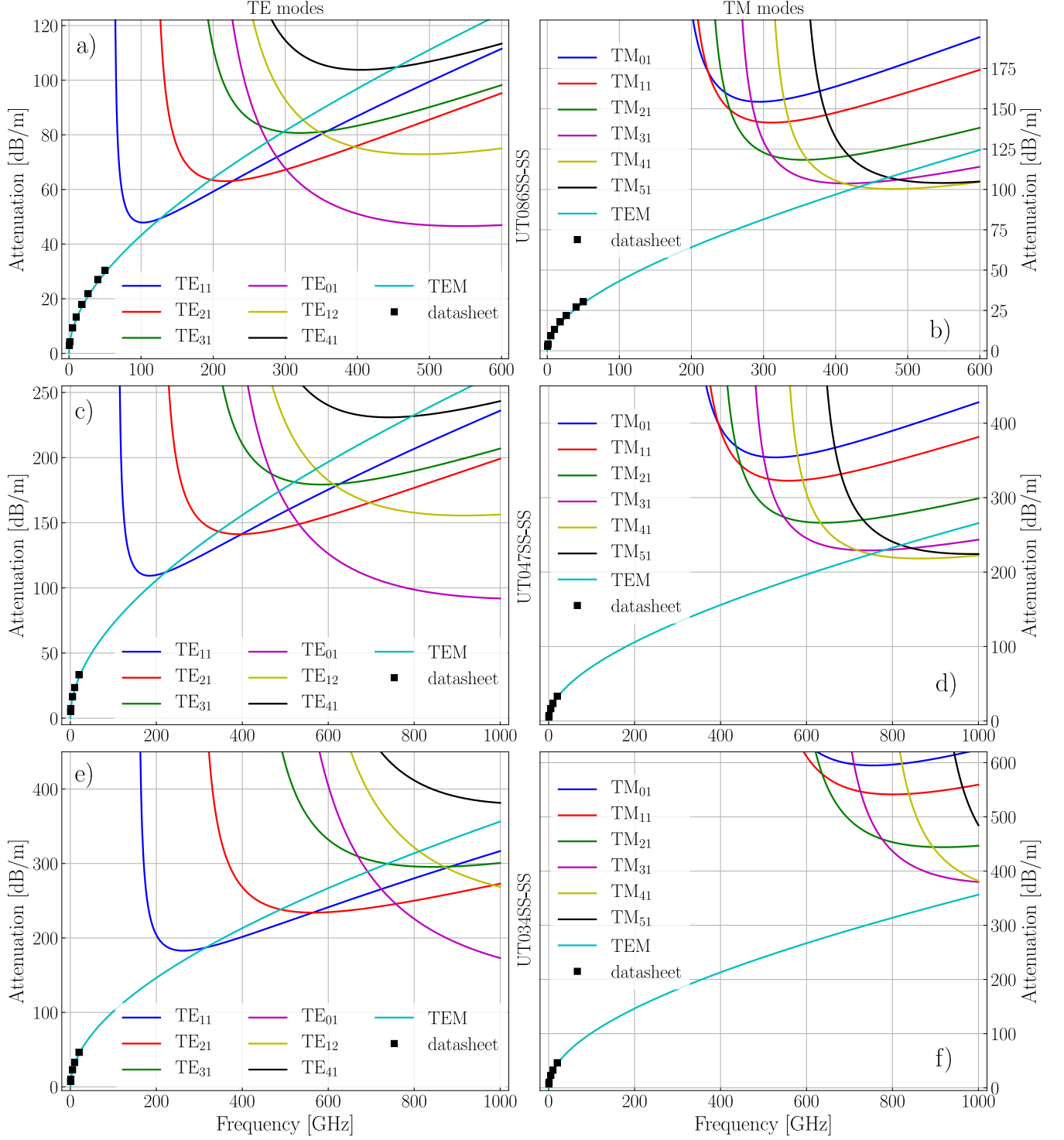


FIG. 1. Attenuation per meter at room temperature for modes with the lowest cut-off frequencies: UT086SS-SS cable (a) TE, (b) TM modes, UT047SS-SS cable (c) TE, (d) TM modes, and UT034SS-SS cable (e) TE, (f) TM modes. Black squares represent the datasheet values for TEM modes.

Numerical solutions of this equation for UT086SS-SS, UT047SS-SS, and UT034SS-SS coaxial cables give us TM modes critical wave-vectors k_c and cut-off frequencies f_c . Six TM modes with the lowest cut-off frequencies are given in the Table II for these types of coaxial cables.

	UT086SS-SS		UT047SS-SS		UT034SS-SS	
TM mode	k_c [1/m]	f_c [GHz]	k_c [1/m]	f_c [GHz]	k_c [1/m]	f_c [GHz]
01	5328	176.4	9464	313.3	13526	447.8
11	5673	187.8	10077	333.6	14392	476.5
21	6575	217.7	11680	386.7	16661	551.6
31	7789	257.9	13837.5	458.1	19721	652.8
41	9134	302.4	16228	537.2	23118	765.3
51	10518	348.2	18686.2	618.6	26616	881.2

TABLE II. Six TM modes of UT086SS-SS, UT047SS-SS, and UT034SS-SS coaxial cables with the lowest cut-off frequencies.

Once the critical wave-vectors k_c are found, we can determine all field components as

$$\begin{aligned}
E_z &= A \cos(n\phi) \left(J_n(k_c \rho) - \frac{J_n(k_c b)}{Y_n(k_c b)} Y_n(k_c \rho) \right) \exp(-j\beta z), \\
E_\rho &= \frac{-j\beta}{k_c} A \cos(n\phi) \left(J'_n(k_c \rho) - \frac{J'_n(k_c b)}{Y'_n(k_c b)} Y'_n(k_c \rho) \right) \exp(-j\beta z), \\
E_\phi &= \frac{j\beta}{k_c^2 \rho} A n \sin(n\phi) \left(J_n(k_c \rho) - \frac{J_n(k_c b)}{Y_n(k_c b)} Y_n(k_c \rho) \right) \exp(-j\beta z), \\
H_\rho &= \frac{-j\omega\epsilon_0\epsilon_r}{k_c^2 \rho} A n \sin(n\phi) \left(J_n(k_c \rho) - \frac{J_n(k_c b)}{Y_n(k_c b)} Y_n(k_c \rho) \right) \exp(-j\beta z), \\
H_\phi &= \frac{-j\omega\epsilon_0\epsilon_r}{k_c} A \cos(n\phi) \left(J'_n(k_c \rho) - \frac{J'_n(k_c b)}{Y'_n(k_c b)} Y'_n(k_c \rho) \right) \exp(-j\beta z).
\end{aligned} \tag{13}$$

With the known field components, we can express the energy flow along the coaxial line P_0 Eq.(6) and the conductor losses per unit length P_l Eq.(7) for TM modes, and the results read

$$\begin{aligned}
P_0 &= \frac{\pi\omega\epsilon_0\epsilon_r \text{Re}\{\beta\} |A|^2}{2k_c^4} \int_{k_c a}^{k_c b} \left[x \left(J'_n(x) - \frac{J_n(k_c b)}{Y_n(k_c b)} Y'_n(x) \right)^2 + \frac{n^2}{x} \left(J_n(x) - \frac{J_n(k_c b)}{Y_n(k_c b)} Y_n(x) \right)^2 \right] dx, \\
P_l &= \frac{\pi R_s \omega^2 \epsilon_0^2 \epsilon_r^2 |A|^2}{2k_c^2} \left[a \left(J'_n(k_c a) - \frac{J_n(k_c b)}{Y_n(k_c b)} Y'_n(k_c a) \right)^2 + b \left(J'_n(k_c b) - \frac{J_n(k_c b)}{Y_n(k_c b)} Y'_n(k_c b) \right)^2 \right].
\end{aligned} \tag{14}$$

Constant A has units of [V/m] in these equations. These quantities can be computed numerically for different TM modes and we get $\alpha_{c,\text{TM}}$ according to the Eq.(5).

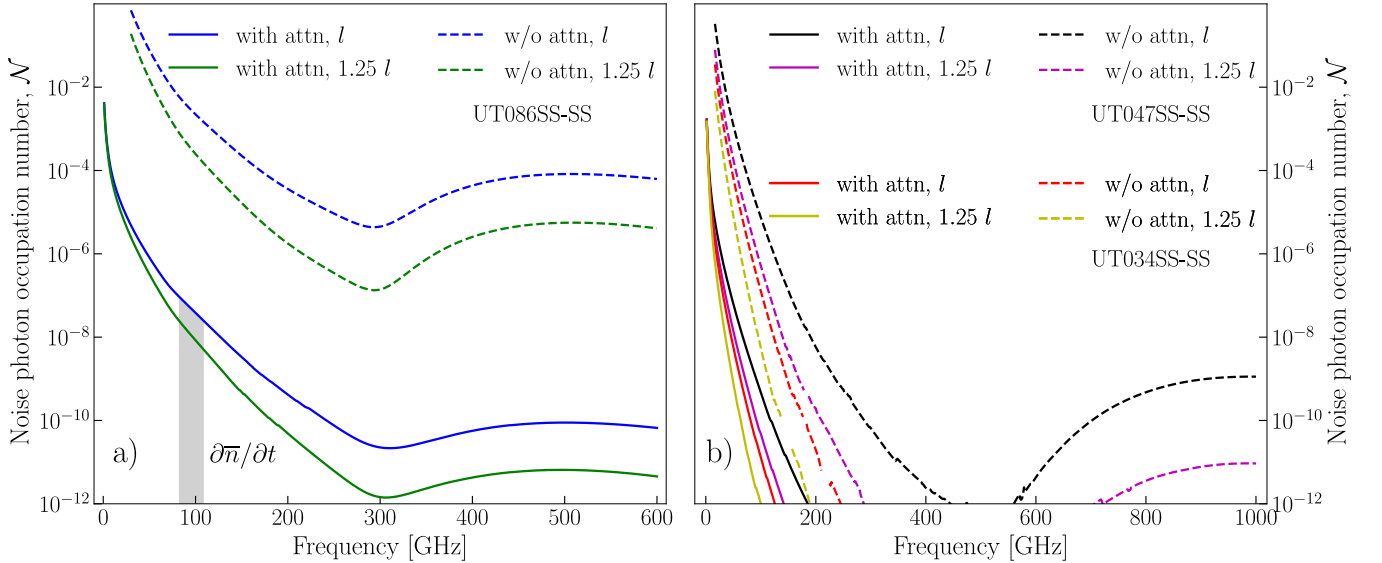


FIG. 2. Estimates of the noise photon occupation numbers for the UT086SS-SS coaxial cable (a) and UT047SS-SS and UT034SS-SS coaxial cables (b). The estimation does not take into account the temperature dependence of the attenuation, and the lines represent the lower bounds of the noise photon occupation numbers.

Attenuation constants related to the dielectric losses for TM modes computed in the same way as for the TE modes in accordance with the Eq.(8) with critical wave-vectors k_c obtained for TM modes. Total attenuation per meter at room temperature for six TM modes with the lowest cut-off frequencies and TEM modes are shown in the Fig.1 for (b) UT086SS-SS, (d) UT047SS-SS, and (f) UT034SS-SS coaxial cables. As can be seen from the Fig. 1, the attenuation of TM modes is considerably higher (by at least 50 dB) than that of TE modes for these types of cables. The contribution of the TM modes to the total flux of noise photons is negligible, and we use only attenuation of TE modes in the estimates of the noise photon flux.

When the total attenuation is known for a given mode, it is possible to estimate the noise photon occupation number for this particular mode at the frequencies of interest as it was explained in Sec. I. Once these numbers are computed for all modes, we can sum up all of them to get the total noise photon occupation number $\mathcal{N}(\omega, x_{\text{end}})$. Fig. 2 shows the estimates of the noise photon occupation numbers at the mixing chamber stage of a dilution refrigerator for UT086SS-SS cable (a) and UT047SS-SS and UT034SS-SS cables (b). The thinner the cable, the higher the attenuation for the same type of mode. As a result, the estimates of the noise photon occupation number is noticeably lower for thinner coaxial cables. The estimates are made for the wiring configuration described in Sec. I. Reduction in the cables attenuation for lower temperatures is not taken into account, and the actual noise photon occupation numbers will be higher than those shown in the Fig. 2. The lines in the Fig. 2 represent the lower bounds of the noise photon occupation numbers. The thinner the cable, the bigger the deviation of the actual noise photon occupation number from the presented values.

III. DETERMINATION OF ELECTROMAGNETIC PROPERTIES OF ESORB-230 MATERIAL

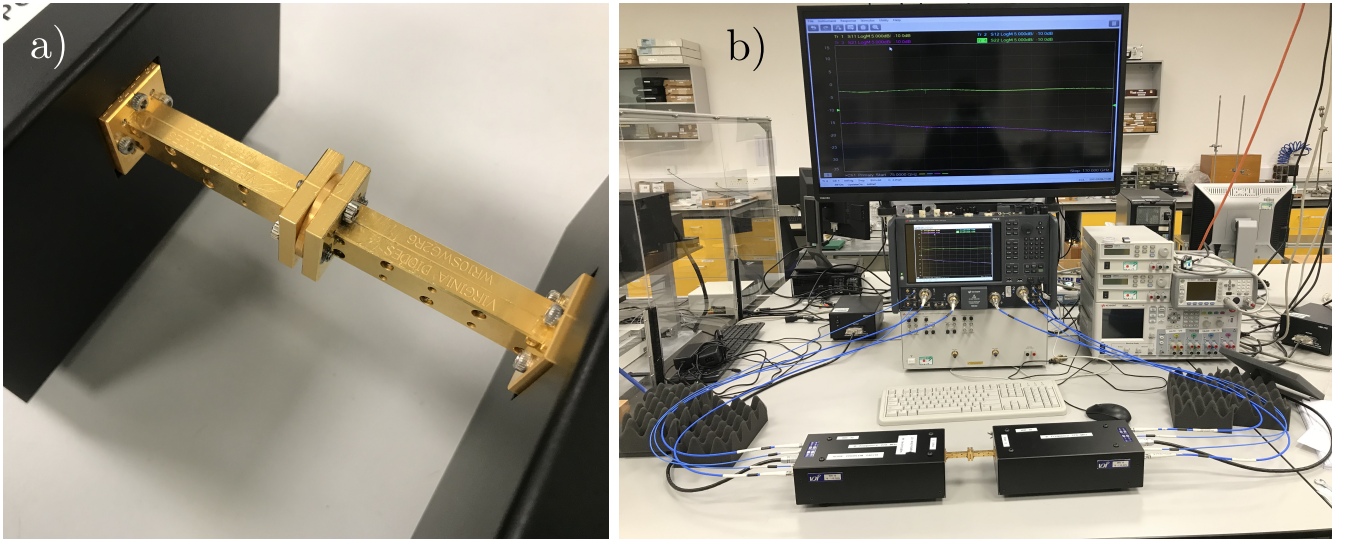


FIG. 3. Measurements of S_{11} and S_{21} scattering parameters of rectangular waveguide sections filled with the Esorb-230 material. (a) The waveguide section placed between the fixtures of the microwave setup. (b) The microwave setup used in the measurements.

Measurements of S_{11} and S_{21} scattering parameters were performed on two thin sections of rectangular waveguides filled with the Esorb-230 absorptive material. Two WR10 waveguides ($2.54 \text{ mm} \times 1.27 \text{ mm}$) with thicknesses 2 mm and 2.7 mm were used in the measurements. Figure 3(a) shows the waveguide section placed between two fixtures of the microwave setup frequency extension modules. The microwave setup operating in the frequency range from 75 to 110 GHz and consisting of a VNA with frequency extension modules is shown in the Fig. 3(b). The system is calibrated to measure with respect to reference planes at the both sides of the waveguide sections. The measured $S_{11}(f)$ and $S_{21}(f)$ parameters are shown in the Fig. 5(b) of the main text.

According to the Nicolson-Ross-Weir method, the complex relative permittivity ϵ_r and permeability μ_r for our experimental setting can be found as

$$\mu_r(f) = \frac{k_z}{\sqrt{(\frac{\omega}{c})^2 - (\frac{\pi}{a})^2} F(f)}, \quad \epsilon_r(f) = \frac{c^2 \left(k_z^2 + (\frac{\pi}{a})^2 \right)}{\omega^2 \mu(f)}, \quad (15)$$

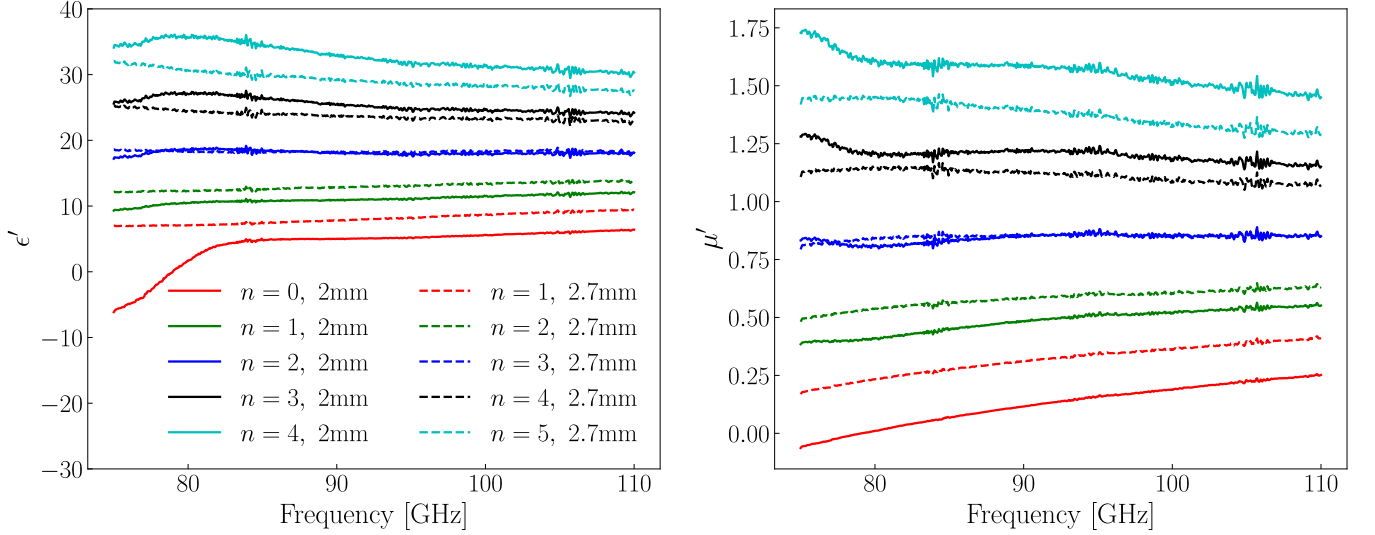


FIG. 4. Real parts of relative dielectric permittivity ϵ' and magnetic permeability μ' of the Esorb-230 material in the frequency range from 75 to 110 GHz determined by the NRW method. Data for two waveguide section thicknesses $d = 2.0$ mm and $d = 2.7$ mm and different solution branches are shown.

where k_z is the component of complex wave-vector along the direction of the waveguide, $a = 2.54$ mm is the bigger side of the rectangular waveguide, and $F(f) = (1 - \Gamma(f))/(1 + \Gamma(f))$. Interfacial reflection coefficient $\Gamma(f)$ is defined as

$$\Gamma(f) = \frac{1 - S_{21}^2 + S_{11}^2}{2S_{11}} + \sqrt{\left(\frac{1 - S_{21}^2 + S_{11}^2}{2S_{11}}\right)^2 - 1}. \quad (16)$$

To compute k_z , we first obtain the propagation factor $P(f)$ as

$$P(f) = |P(f)|e^{j\phi(f)} = \frac{S_{21}(f) - S_{11}(f) + \Gamma(f)}{1 + \Gamma(f)(S_{21}(f) - S_{11}(f))} = e^{-jk_z d}, \quad (17)$$

where d is the thickness of the waveguide section filled with the absorptive material. From here,

$$\text{Re}(k_z) = \frac{2\pi n - \phi(f)}{d}, \quad \text{and} \quad \text{Im}(k_z) = \frac{\ln |P(f)|}{d}. \quad (18)$$

The phase of the propagation factor is 2π periodic, and, as a result, the real part of the wave-vector depends on the unknown integer n enumerating the solution branch. That is where the ambiguity of the method arises.

The dielectric and magnetic loss tangents are found from ϵ_r and μ_r as

$$\tan(\delta) = -\frac{\text{Im}(\epsilon_r)}{\text{Re}(\epsilon_r)}, \quad \text{and} \quad \tan(\delta_m) = -\frac{\text{Im}(\mu_r)}{\text{Re}(\mu_r)}. \quad (19)$$

We calculate the real parts of dielectric permittivity $\epsilon' = \text{Re}(\epsilon_r)$ and magnetic permeability $\mu' = \text{Re}(\mu_r)$ for both waveguide sections with thicknesses $d = 2.0$ mm and $d = 2.7$ mm and different branch indexes n , see Fig. 4. Electromagnetic parameters should not depend on the section thickness, and this allows for the resolution of the ambiguity. Namely, the real parts ϵ' and μ' determined for $n = 2$ and $d = 2.0$ mm and for $n = 3$ and $d = 2.7$ mm closely coincide in contrast to the solutions for the other branches. The loss tangents given by the imaginary parts of ϵ_r and μ_r are much smaller, and the branch selection is made based on the real parts of the quantities. The final values of all electromagnetic parameters of Esorb-230 material (ϵ' , μ' , $\tan(\delta)$, $\tan(\delta_m)$) are taken as mean values of the solutions for these two branches.

IV. ATTENUATION CONSTANT OF THE ESORB-230 FILTER

Only two electromagnetic modes are supported by the UT086SS-SS coaxial line in the frequency range from 75 to 110 GHz. These are TEM and TE_{11} modes. With the knowledge of electromagnetic parameters of the Esorb-230

material and the geometric parameters of the filter, it is possible to estimate the attenuation constants for these two modes similar to the way it was done earlier for the coaxial line. We compute the critical wave-vector $k_c = 645$ 1/m and the cut-off frequency $f_c = 8.1$ GHz for the TE_{11} mode. The values are reduced in comparison to the coaxial line due to the bigger diameters of the inner and outer conductors of the filter and the bigger relative dielectric constant of the absorptive material.

With the known electromagnetic fields inside the filter, we can compute the integrals P_0 Eq. (6) and P_l Eq. (7) for both modes to estimate the attenuation related to the conductor losses per unit length of the filter α_c [dB/m] = $20 \log_{10}(e) \cdot (P_l/2P_0)$. Room temperature value of Copper conductivity $\sigma_{Cu,RT} \simeq 67 \cdot 10^6$ S/m was used in the surface resistance estimation. The obtained results are shown in the Fig. 5(a). Loss tangents of Esorb-230 material are not small, and we find the dielectric P_d and magnetic P_m losses per unit length of the filter computing the integrals

$$P_d = \frac{\omega}{2} \int_{\rho=a}^b \int_0^{2\pi} \epsilon'' |\vec{E}|^2 \rho d\phi d\rho \quad \text{and} \quad P_m = \frac{\omega}{2} \int_{\rho=a}^b \int_0^{2\pi} \mu'' |\vec{H}|^2 \rho d\phi d\rho. \quad (20)$$

Here, $\epsilon'' = \epsilon_r \tan(\delta)$ and $\mu'' = \mu_r \tan(\delta_m)$ are the imaginary parts of the dielectric permittivity and the magnetic permeability. The attenuation related to the material losses per unit length is found as α_{dm} [dB/m] = $20 \log_{10}(e) \cdot ((P_d + P_m)/2P_0)$. The results are shown in the Fig. 5(b).

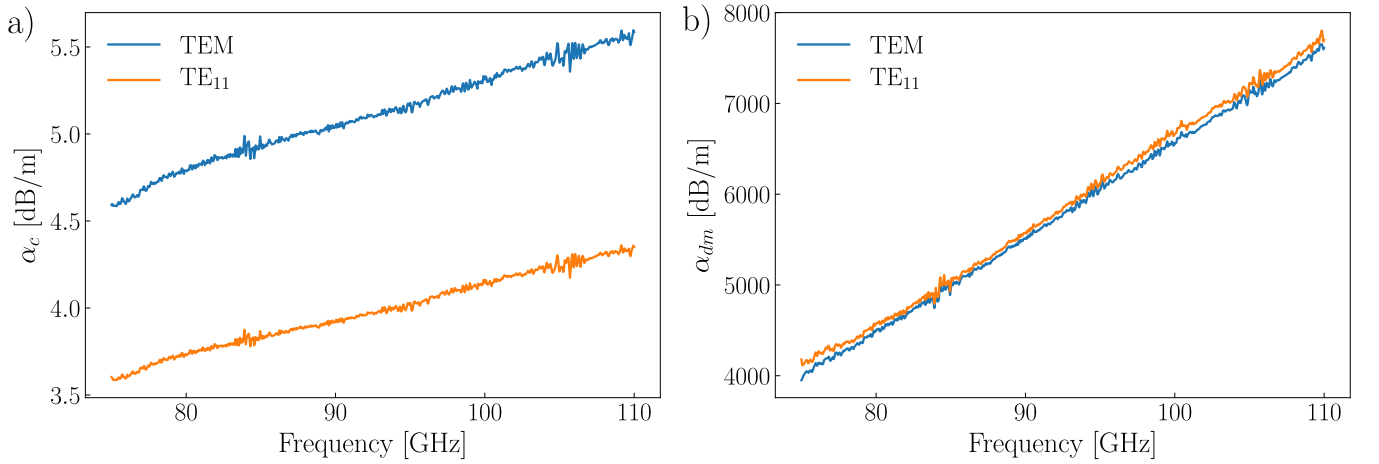


FIG. 5. Attenuation constants of the filter for TEM and TE_{11} modes due to (a) conductor losses and (b) dielectric and magnetic losses in the Esorb-230 material.

Attenuation constants given in the Eq. (9) and the Eq. (8) are good approximations for the case when losses in insulating material of a coaxial line are small. We found that the attenuation constants computed with the use of these equations deviate only a little bit from the constants presented in Fig. 5 for the entire studied frequency range. The deviation is not exceeding 3.7%.

Conductor losses are about three orders of magnitude lower than the dielectric and magnetic losses and can be neglected in the consideration of filter attenuation. Dielectric and magnetic losses for TEM and TE_{11} modes are very similar due to the small value of the critical wave-vector k_c for the TE_{11} mode in comparison to the wave-vectors for the considered frequency range.